2016

Mode-converted ultrasonic scattering in polycrystals with elongated grains

Andrea P. Arguelles
U.S. Army Research Laboratory, Aberdeen

Christopher M. Kube
U.S. Army Research Laboratory, Aberdeen

Ping Hu
Wuhan University

Joseph A. Turner
University of Nebraska-Lincoln, jaturner@unl.edu

Mode-converted ultrasonic scattering in polycrystals with elongated grains

Andrea P. Arguelles, Christopher M. Kube,[a] Ping Hu,[b] and Joseph A. Turner[c]
Department of Mechanical and Materials Engineering, University of Nebraska-Lincoln, W342 Nebraska Hall, Lincoln, Nebraska 68588-0526, USA

(Received 9 March 2016; revised 16 August 2016; accepted 20 August 2016; published online 8 September 2016)

Elastic wave scattering is used to study polycrystalline media for a wide range of applications. Received signals, which include scattering from the randomly oriented grains comprising the polycrystal, contain information from which useful microstructural parameters may often be inferred. Recently, a mode-converted diffuse ultrasonic scattering model was developed for evaluating the scattered response of a transverse wave from an incident longitudinal wave in a polycrystalline medium containing equiaxed single-phase grains with cubic elastic symmetry. In this article, that theoretical mode-converted scattering model is modified to account for grain elongation within the sample. The model shows the dependence on scattering angle relative to the grain axis orientation. Experimental measurements were performed on a sample of 7475-T7351 aluminum using a pitch-catch transducer configuration. The results show that the mode-converted scattering can be used to determine the dimensions of the elongated grains. The average grain shape determined from the experimental measurements is compared with dimensions extracted from electron backscatter diffraction, an electron imaging technique. The results suggest that mode-converted diffuse ultrasonic scattering has the potential to quantify detailed information about grain microstructure.
 [http://dx.doi.org/10.1121/1.4962161]

[ANN] Pages: 1570–1580

I. INTRODUCTION

Ultrasonic scattering in a polycrystal occurs as a wave propagates through grain boundaries resulting from the crystallogaphic misorientation of adjacent grains. Although the goal for flaw detection applications is generally to minimize such scattering, this signal contains valuable information about the material microstructure. Multiple studies have focused on scattering quantification techniques to measure microstructural properties. Early research focused on the diffusion limit, where multiple scattering events and attenuation dominate the response for depths well into the material.[1–5] Initial models based on single scattering events from equiaxed grains were developed by Rose[6–8] and Margetan *et al.*[9]

Manufacturing processes often induce a preferred direction of grain elongation which motivated researchers to extend spherical grain scattering models to ellipsoidal grains. Ahmed and Thompson[10] followed an approach similar to Rose[6–8] and Margetan[9] to define longitudinal scattering from polycrystals with ellipsoidal grains of circular cross-section; the effect of elongation was included by modifying the spatial correlation function which defines the spatial dependence of the grain statistics. Later, Han and Thompson[11] followed a similar formalism to study the case of polycrystals with duplex microstructures. Guo *et al.*[12,13] described backscatter experiments on a rolled aluminum sample and used a least squares optimization method to determine the two average radii for the major and minor axes when fitting the data with Han's model.[11] More recent studies have focused on polycrystals that include grains with elongation in two directions, resulting in three independent grain radii.[14,15] Lobkis *et al.*[14,15] extended that work to extract ellipsoidal radii and a microtexture parameter from experiments that used longitudinal backscatter at normal incidence on three faces of a rectangular sample. Their work has been further extended to include macroscopic anisotropy and grains of more general crystallographic point group symmetries.[16–20] However, these models[14–20] are based on a plane wave assumption, neglecting the beam behavior inherent when focused transducers are used.

The issue of proper beam modeling was addressed by Ghoshal *et al.*,[21] who utilized Wigner transforms to describe the transducer beam patterns for both the source and receiver. Ghoshal and Turner[22] followed with a model specific for the case of longitudinal scattering in a pulse-echo configuration through planar and curved interfaces. Hu *et al.*[23] expanded to the case of longitudinal-to-shear (L-T) scattering, all for equiaxed grains. Mode-conversion is advantageous due to the absence of a coherent front surface reflection in the measured signal, which allows inspection depths closer to the surface. Additionally, mode-converted inspections may improve the detectability of defects elongated perpendicular to the surface, such as microcracks or fatigue damage. Scattering experiments specifically,[21–23] improve on approaches based on attenuation because they can separate the effects of scattered longitudinal and transverse

[a]Current address: Mechanics Division, Vehicle Technology Directorate, U.S. Army Research Laboratory, Aberdeen Proving Ground, Aberdeen, MD 21005, USA.
[b]Current address: School of Power and Mechanical Engineering, Wuhan University, Wuhan, Hubei 430072, China.
[c]Electronic mail: jaturner@unl.edu

energy and the thickness of the sample does not need to be determined *a priori*.

In this article, the mode conversion model by Hu *et al.*[23] is expanded to include ellipsoidal grain shape and arbitrary grain orientation relative to the measurement. The spatial correlation function is modified to include three independent grain radii and a separate coordinate system is assigned for the grains. The inclusion of arbitrary grain orientation in the model presents an opportunity to test the sample through a single surface in order to determine elongation, improving on previous models for which accessibility to more than one surface was necessary.[14,15] Numerical examples for the model are presented for an aluminum sample to illustrate the effects of elongation ratio, rotation of the grains about two directions, and orientation of the oblique receiving transducer. The model is then used to extract three ellipsoidal grain radii and grain orientation from experimental scattering measurements on a rolled aluminum sample.

II. REVIEW OF MODE-CONVERTED ULTRASONIC SCATTERING

Ghoshal *et al.*[21] first derived an analytical expression for the time-dependent spatial variance of signals captured at various positions on a sample under a single scattering assumption. This variance, referred to as the singly-scattered response or SSR, is given by

$$\Phi(t) = \gamma_S \gamma_R \int \frac{d\omega}{(2\pi)^4} d\mathbf{k} d\mathbf{k}' d\mathbf{x} dt' \times W^R_{\beta j}(\mathbf{x}, t-t', \mathbf{k}', \omega) {}^{\mathbf{k}'\beta}_{\mathbf{k}'j} K^{\gamma\mathbf{k}}_{k\mathbf{k}} W^S_{\gamma k}(\mathbf{x}, t', \mathbf{k}, \omega). \quad (1)$$

Equation (1) is an integral of the inner product of $\mathbf{W}^S$ and $\mathbf{W}^R$ with the intensity operator $\mathbf{K}$ associated with the heterogeneous medium, and includes a temporal convolution of $\mathbf{W}^S$ and $\mathbf{W}^R$. $\mathbf{W}^S$ and $\mathbf{W}^R$ are the transducer energy distributions, quantified by the four-fold Wigner transform of the corresponding displacement fields created by the transducer, for the source and receiver, respectively. More specifically, $\mathbf{W}$ represents the signal in the space-time ($\mathbf{x}$, t) and wave vector-frequency ($\mathbf{k}$, ω) domains simultaneously. γ_S and γ_R are obtained through calibration experiments; they relate the displacement fields to the transducer voltages. The intensity operator $\mathbf{K}$ is an eighth-rank tensor that quantifies the scattering within the material and is often expressed in the contracted form

$$ {}^{\mathbf{k}'\beta}_{\mathbf{k}'j} K^{\gamma\mathbf{k}}_{k\mathbf{k}} \approx \tilde{\eta}(\mathbf{k}'-\mathbf{k}) \mathbf{k}'_\alpha \mathbf{k}_\delta \mathbf{k}'_l \mathbf{k}_m \Xi^{\alpha\delta\beta\gamma}_{lmjk} = k'^2 k^2 \tilde{\eta}(k'\hat{\mathbf{k}}' - k\hat{\mathbf{k}}) \hat{k}'_\alpha \hat{k}_\delta \hat{k}'_l \hat{k}_m \Xi^{\alpha\delta\beta\gamma}_{lmjk} \quad (2)$$

assuming the spatial and tensorial components are independent of each other.[24] The notation ${}^{\mathbf{k}'\beta}_{\mathbf{k}'j} K^{\gamma\mathbf{k}}_{k\mathbf{k}}$ denotes a wave propagating in the $\hat{\mathbf{k}}$ direction that scatters into the $\hat{\mathbf{k}}'$ direction. The function $\tilde{\eta}(\mathbf{k}'-\mathbf{k})$ is the spatial Fourier transform of the two-point probability function giving the likelihood that two randomly chosen positions will lie within a given grain. Hence, $\tilde{\eta}$ is a function of the difference between the incident and scattered wave vectors due to the implicit assumption of statistical homogeneity. The spatial correlation function for the case of ellipsoidal grains is further explained in Sec. III. $\Xi^{\alpha\delta\beta\gamma}_{lmjk}$ is the elastic modulus covariance given by $\Xi^{\alpha\delta\beta\gamma}_{lmjk} = \langle C_{lmjk} C_{\alpha\delta\beta\gamma} \rangle - \langle C_{lmjk} \rangle \langle C_{\alpha\delta\beta\gamma} \rangle$, which represents the second-order statistics of the spatial distribution of crystal orientations responsible for the scattering.

The general expression given in Eq. (1) allows for mode conversion between the incident and scattered fields. In this article, the transducer configuration is restricted to the case of a normal incidence longitudinal wave and a scattered shear wave, as shown in Fig. 1 (the reciprocal case is equivalent). The foci of the transducers are chosen to overlap by adjusting the water and material paths for the source (z_{fS} and z_S) and the receiver (z_{fR} and z_R). The Wigner transform of a piston transducer was first given by Ghoshal *et al.*[21] and explicitly written for longitudinal propagation in Ghoshal and Turner.[22] This expression, corresponding to $\mathbf{W}^S$ in the present transducer configuration, is given by

$$W^S_{\gamma k}(\mathbf{x}, t, \mathbf{k}, \omega) = T^2_{fL} A^2_{0S} (2\pi)^3 \sqrt{2\pi} \sigma_S \frac{w^2_{0S}}{w_1(z) w_2(z)} \times \exp\left[-\frac{2x^2}{w^2_1(z)} - \frac{2y^2}{w^2_2(z)} \right] \times \exp\left[-\frac{2z(z-2tc_L)}{\sigma^2_S c^2_L} - 2\alpha_L z - 2\left(\frac{t}{\sigma_S}\right)^2 - \frac{1}{2}\sigma^2_S(\omega-\omega_{0S})^2 \right] \times \delta^3(\mathbf{k}-\mathbf{k}_0) \hat{e}_\gamma \hat{e}_k (\hat{\mathbf{k}} \cdot \hat{\mathbf{n}}_S)^2. \quad (3)$$

The source transducer coordinates $\mathbf{x}$ are chosen to correspond with the global coordinate system. Then, as reported by Hu *et al.*,[23] the receiver Wigner transform can be cast in a form similar to Eq. (3) using a local coordinate system $\mathbf{X}$

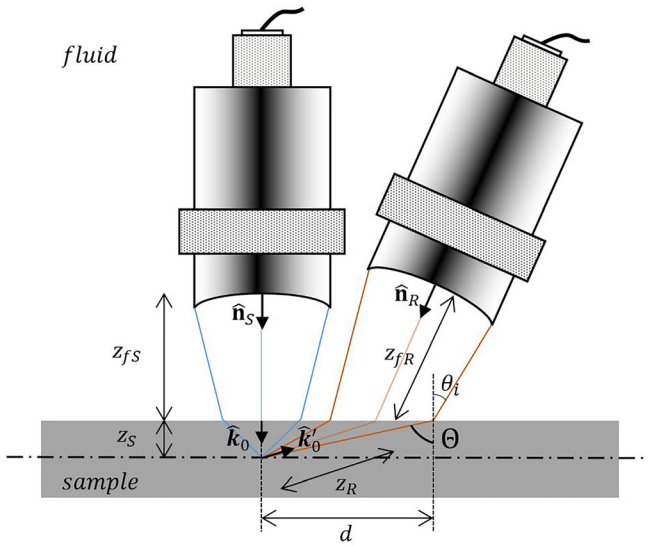

FIG. 1. (Color online) Schematic diagram of a pitch-catch transducer configuration, where the source transducer is at normal incidence and the receiving transducer is at oblique incidence.

and shear wave properties for the case of a scattered shear wave, so that

$$W^R_{\beta j}(\mathbf{X},t,\mathbf{k}',\omega) = T^2_{Tf}A^2_{0R}(2\pi)^4\frac{w^2_{0R}}{w_1(Z)w_2(Z)} \times \exp\left[-\frac{2X^2}{w_1^2(Z)}-\frac{2y^2}{w_2^2(Z)}\right] \times \exp\left[-\frac{2Z(Z-2tc_T)}{\sigma_R^2c_T^2} - 2\alpha_T Z - 2\left(\frac{t}{\sigma_R}\right)^2\right]\delta(\omega-\omega_{0R}) \times \delta^3(\mathbf{k}'-\mathbf{k}'_0)\hat{e}'_\beta\hat{e}'_j\left(\hat{\mathbf{k}}'\cdot\hat{\mathbf{n}}_R\right)^2. \quad (4)$$

In order to simplify later integrations, the receiving transducer is assumed to have a single frequency ω_{0R} rather than a Gaussian distribution of frequencies.[21–23] In Eqs. (3) and (4), A_0 is an amplitude correction due to propagation in the fluid;[25] T_{fL} and T_{Tf} are the transmission coefficients of the longitudinal wave from the fluid to the sample and of the shear wave from the sample to the fluid;[25] c_L and c_T, α_L and α_T, are the wave speeds and attenuations for the longitudinal and transverse (shear) waves; and σ_S and σ_R, ω_{0S} and ω_{0R} are the pulse widths and center frequencies for the source and receiving transducers, respectively. $\mathbf{k}$ and $\mathbf{k}'$ correspond with the propagation vectors for the incident and scattered waves; $\hat{\mathbf{e}}$ and $\hat{\mathbf{e}}'$ represent the displacement directions for the incident and scattered waves; and $\hat{\mathbf{n}}_S$ and $\hat{\mathbf{n}}_R$ are the unit vectors normal to the surface of the source and receiving transducers, respectively. Theoretical calculation of the attenuation coefficients for elongated grains needed for the results presented in Secs. IV and V is achieved by modifying Kube and Turner's model[26] to the case of elongated grains using Euler angles with an approach similar to that given in Sec. III.

The Wigner transforms in Eqs. (3) and (4) are derived under a single Gaussian beam assumption in space for the piston transducers,[21] such that w_0 is the initial beam width, and $w_1(z)$ and $w_2(z)$ are the widths of the Gaussian profile along the propagation axis z.[27] Restricting the analysis to a planar surface, the single Gaussian beam parameters are given by[22,27]

$$\frac{1}{q_\xi(z_\xi)} = \frac{1}{R_\xi(z_\xi)} - i\frac{2}{k_f w^2_\xi(z_\xi)},$$
$$q_{1\xi}(z_\xi) = \frac{\cos^2\theta_{\xi r}}{\cos^2\theta_{\xi i}}\left[q_\xi(0)+z_{f\xi}\right]+\frac{c_\chi}{c_f}z_\xi,$$
$$q_{2\xi}(z_\xi) = q_\xi(0)+z_{f\xi}+\frac{c_\chi}{c_f}z_\xi. \quad (5)$$

The subscript ξ is used to differentiate the transducers ($\xi = S, R$, source or receiver, respectively) and the subscript χ corresponds with the wave type ($\chi = L, T$, longitudinal or transverse, respectively). $z_S = z$ and $z_R = Z$, which are the source and receiver propagation axes, respectively. θ_i is the angle of incidence of each transducer and θ_r is the refraction angle calculated using Snell's law. For the source transducer at normal incidence $\theta_i = \theta_r$ [yielding $q_{1S}(z) = q_{2S}(z) = q_S(z)$] and for the receiver $\theta_r = \Theta$. $R_\xi(0) = -F$ and $w_\xi(0) = w_{0\xi} = 0.7517a$ are the initial radius and beam width of the wavefront, respectively, where F is the focal length of the transducer in the fluid and a is the nominal radius of the transducer element.[27] $k_{f\xi} = \omega_{0\xi}/c_f$ is the wave number of the immersion fluid taken at the center frequency of the source and receiving transducers accordingly. Then, the widths of the single Gaussian beam can be written as

$$w_1^2(z) = w_2^2(z) = w^2(z) = -\frac{2}{k_f\mathrm{Im}\left(1/q_S(z)\right)};$$
$$w_1^2(Z) = -\frac{2}{k_f\mathrm{Im}\left(1/q_{1R}(Z)\right)},$$
$$w_2^2(Z) = -\frac{2}{k_f\mathrm{Im}\left(1/q_{2R}(Z)\right)}, \quad (6)$$

for the source and receiver, respectively. Because the spatial integration in Eq. (1) is in the global coordinate system $\mathbf{x}$, a coordinate transformation from $\mathbf{X}$ to $\mathbf{x}$ is necessary and can be found in Hu *et al.*[23] Now Eqs. (3) and (4) can be substituted into Eq. (1). Generally, transducers used for these experiments are of matched frequencies and pulse width; hence, we can assume $\sigma_S = \sigma_R = \sigma$ and $\omega_{0S} = \omega_{0R} = \omega_0$ and obtain

$$\Phi(t) = \gamma_S\gamma_R(T_{fL}T_{Tf})^2(A_{0R}A_{0S})^2(2\pi)^3\sqrt{2\pi}\sigma\int d\omega d\mathbf{k}d\mathbf{k}'dxdydzdt'\frac{w^2_{0R}w^2_{0S}}{w^2(z)w_1(Z)w_2(Z)} \times \exp\left[-\frac{2X^2}{w_1^2(Z)}-\frac{2y^2}{w_2^2(Z)}-\frac{2Z(Z-2(t-t')c_T)}{\sigma^2c_T^2}-2\alpha_TZ-2\left(\frac{t-t'}{\sigma}\right)^2\right] \times \exp\left[-\frac{1}{2}\sigma^2(\omega-\omega_0)^2\right]\delta^3(\mathbf{k}'-\mathbf{k}'_0)\hat{e}'_\beta\hat{e}'_j\left(\hat{\mathbf{k}}'\cdot\hat{\mathbf{n}}_R\right)^2k'^2k^2\tilde{\eta}\left(k'\hat{\mathbf{k}}'-k\hat{\mathbf{k}}\right)\hat{k}'_\alpha\hat{k}_\delta\hat{k}'_l\hat{k}_m\Xi^{\alpha\delta\beta\gamma}_{lmjk} \times \exp\left[-\frac{2x^2}{w^2(z)}-\frac{2y^2}{w^2(z)}-\frac{2z(z-2t'c_L)}{\sigma^2c_L^2}-2\alpha_Lz-2\left(\frac{t'}{\sigma}\right)^2\right] \times \delta(\omega-\omega_0)\delta^3(\mathbf{k}-\mathbf{k}_0)\hat{e}_\gamma\hat{e}_k\left(\hat{\mathbf{k}}\cdot\hat{\mathbf{n}}_S\right)^2. \quad (7)$$

Integrating in the temporal dimension t', in the out-of-plane dimension y, over wave vectors $\mathbf{k}$ and $\mathbf{k}'$, and frequency ω, gives

$$\Phi(t) = \gamma_S\gamma_R(T_{fL}T_{Tf})^2(A_{0R}A_{0S})^2(2\pi)^3\frac{\omega_0^4}{c_L^2c_T^2}\sigma^2\frac{\pi\sqrt{\pi}}{2}\int dxdz\frac{w_{0R}^2w_{0S}^2}{w(z)w_1(Z)\sqrt{w^2(z)+w_2^2(Z)}}\exp\left[-\frac{2X^2}{w_1^2(Z)}-\frac{2x^2}{w^2(z)}\right]$$
$$\times\exp\left[-2\alpha_TZ-2\alpha_Lz-\frac{2Z(Z-2tc_T)}{\sigma^2c_T^2}-\frac{2z^2}{\sigma^2c_L^2}\right]$$
$$\times\exp\left[-2\left(\frac{t}{\sigma}\right)^2+\frac{1}{\sigma^2}\left(\frac{z}{c_L}-\frac{Z}{c_T}+t\right)^2\right]\tilde{\eta}\left(k'\hat{\mathbf{k}}_0'-k\hat{\mathbf{k}}_0\right)\hat{k}_\alpha'\hat{k}_\delta\hat{k}_l'\hat{k}_m\Xi_{lmjk}^{\alpha\delta\beta\gamma}\hat{e}_\gamma\hat{e}_k\left(\hat{\mathbf{k}}_0\cdot\hat{\mathbf{n}}_S\right)^2\hat{e}_\beta'\hat{e}_j'\left(\hat{\mathbf{k}'}_0\cdot\hat{\mathbf{n}}_R\right)^2. \quad (8)$$

On the basis of the unit vector relationships depicted in Fig. 1, we find that $\hat{\mathbf{k}}_0\cdot\hat{\mathbf{n}}_S=1$ and $\hat{\mathbf{k}}_0'\cdot\hat{\mathbf{n}}_R=-\cos(\Theta-\theta_i)$. The coefficients γ_ξ and $A_{0\xi}$ are given by

$$\gamma_S = V_{\max}^S\frac{2\rho_fk_f^2\sigma c_f^2}{R_{ff}D_S(\omega_0)}\sqrt{\frac{2}{\pi}}\frac{w(z_{FS})}{w_{0S}^2}\left(\pi w_{0S}^2\right)^2\exp(2\alpha_fz_{FS}),$$
$$\gamma_R = V_{\max}^R\frac{2\rho_fk_f^2\sigma c_f^2}{R_{ff}D_R(\omega_0)}\sqrt{\frac{2}{\pi}}\frac{w(z_{FR})}{w_{0R}^2}\left(\pi w_{0R}^2\right)^2\exp(2\alpha_fz_{FR}), \quad (9)$$

$$A_{0S} = -\frac{\exp(-\alpha_fz_{fS})}{4\pi w_{0S}^2\rho_fc_f^2\sigma k_f\sqrt{\pi}},\quad A_{0R} = -\frac{\exp(-\alpha_fz_{fR})}{4\pi w_{0R}^2\rho_fc_f^2\sigma k_f\sqrt{\pi}}, \quad (10)$$

where $V_{\max}^\xi$ are the maximum signal voltages for the individual transducers (assuming reflection off a planar surface at normal incidence). Details of the calibration procedure can be found elsewhere.[22] $R_{ff}=(\rho c_L-\rho_fc_f)/(\rho c_L+\rho_fc_f)$ is the reflection coefficient and $D_\xi(\omega_0)=|1-e^{-(2\pi i/s_\xi)}[J_0(2\pi/s_\xi)+iJ_1(2\pi/s_\xi)]|$ is the diffraction correction constant[28] where $s_\xi=4\pi c_fz_{F\xi}/\omega_0w_{0\xi}^2$. Finally, Eq. (8) becomes

$$\Phi(t) = \Phi_0(t)B\int dxdz\frac{1}{w(z)w_1(Z)\sqrt{w^2(z)+w_2^2(Z)}}$$
$$\times\exp\left[-\frac{2X^2}{w_1^2(Z)}-\frac{2x^2}{w^2(z)}\right]$$
$$\times\exp\left[-\frac{2Z(Z-2tc_T)}{\sigma^2c_T^2}-\frac{2z^2}{\sigma^2c_L^2}\right.$$
$$\left.+\frac{1}{\sigma^2}\left(\frac{z}{c_L}-\frac{Z}{c_T}\right)^2+\frac{2}{\sigma^2}\left(\frac{z}{c_L}-\frac{Z}{c_T}\right)t\right]$$
$$\times\exp[-2\alpha_TZ-2\alpha_Lz], \quad (11)$$

where

$$\Phi_0(t) = \frac{\pi\sqrt{\pi}}{8}V_{\max}^SV_{\max}^R\left(\frac{T_{fL}T_{Tf}}{R_{ff}}\right)^2\left(\frac{1}{\rho_fc_f^2}\right)^2$$
$$\times\frac{w(z_{FS})w(z_{FR})}{D_S(\omega_0)D_R(\omega_0)}\cos^2(\Theta-\theta_i)$$
$$\times\exp\left[2\alpha_f(z_{FS}-z_{fS})\right]\exp\left[2\alpha_f(z_{FR}-z_{fR})\right]$$
$$\times\exp\left[-\left(\frac{t}{\sigma}\right)^2\right] \quad (12)$$

is a factor related to experiment calibration and B is the scattering coefficient explained in Sec. III.

III. SCATTERING COEFFICIENT FOR ELONGATED GRAINS

The expression given by Eq. (11) is applicable to materials with various microstructures. In this article, the case of preferred grain elongation without texture is considered, for which the scattering coefficient is given by

$$B = \left(\frac{\omega_0^2}{c_Lc_T}\right)^2\tilde{\eta}\left(k'\hat{\mathbf{k}}_0'-k\hat{\mathbf{k}}_0\right)\hat{k}_\alpha'\hat{k}_\delta\hat{e}_\beta'\hat{e}_\gamma\hat{k}_l'\hat{k}_m\hat{e}_j'\hat{e}_k\Xi_{lmjk}^{\alpha\delta\beta\gamma}. \quad (13)$$

The term $\hat{k}_\alpha'\hat{k}_\delta\hat{e}_\beta'\hat{e}_\gamma\hat{k}_l'\hat{k}_m\hat{e}_j'\hat{e}_k\Xi_{lmjk}^{\alpha\delta\beta\gamma}$ can be reduced for the case of cubic single crystal symmetry. Assuming Voigt averaging of the elastic moduli and using the transducer configuration given in Fig. 1 gives[23,29,30]

$$\hat{k}_\alpha'\hat{k}_\delta\hat{e}_\beta'\hat{e}_\gamma\hat{k}_l'\hat{k}_m\hat{e}_j'\hat{e}_k\Xi_{lmjk}^{\alpha\delta\beta\gamma} = \frac{\nu^2}{4200}(81-\cos 4\Theta), \quad (14)$$

where $\nu=c_{11}-c_{12}-2c_{44}$ is the anisotropy coefficient with c_{11}, c_{12}, and c_{44} as the single crystal elastic constants and Θ is the angle between the incident and scattered waves in the material. The inner products of the covariance with the displacement and propagation vectors for triclinic and hexagonal crystal symmetries are included in the Appendix. The correlation function η represents the probability that two randomly chosen positions lie within a given grain. The spatial Fourier transform of the correlation function can be written in terms of the unit vectors $\hat{\mathbf{k}}_0$ and $\hat{\mathbf{k}}_0'$, given in Fig. 1, or in terms of the global coordinate system as

$$\tilde{\eta}(\mathbf{q}) = \tilde{\eta}(k'\hat{\mathbf{k}}_0'-k\hat{\mathbf{k}}_0) = \tilde{\eta}(q_x\hat{\mathbf{x}}+q_y\hat{\mathbf{y}}+q_z\hat{\mathbf{z}}). \quad (15)$$

Then, for the case of ellipsoidal grains, the correlation function reduces to

$$\tilde{\eta} = \tilde{\eta}(\mathbf{q}) = \frac{a_xa_ya_z}{\pi^2\left(1+a_x^2q_x^2+a_y^2q_y^2+a_z^2q_z^2\right)^2}, \quad (16)$$

where a_x, a_y, and a_z define the radii of the ellipsoid in the x, y, and z directions, respectively. Because the directions of unit vectors $\hat{\mathbf{k}}_0$ and $\hat{\mathbf{k}}_0'$ are known, we can write

$$q_x = (k'\hat{\mathbf{k}}_0' - k\hat{\mathbf{k}}_0)\cdot\hat{\mathbf{x}} = k'\sin\Theta,$$
$$q_y = (k'\hat{\mathbf{k}}_0' - k\hat{\mathbf{k}}_0)\cdot\hat{\mathbf{y}} = 0, \quad \text{and}$$
$$q_z = (k'\hat{\mathbf{k}}_0' - k\hat{\mathbf{k}}_0)\cdot\hat{\mathbf{z}} = -k'\cos\Theta - k, \tag{17}$$

where $k = \omega_0/c_L$ is the wave number of an incident longitudinal wave, $k' = \omega_0/c_T$ is the wave number of a scattered shear wave and Θ is the angle between the incident and scattered waves in the material. A new coordinate system is defined for the ellipsoidal grains in order to allow arbitrary directions of elongation with respect to the transducer configuration. The relation between the global axes (x,y,z) and the grain axes (X_g, Y_g, Z_g) can be specified using three Euler angles ψ_g, θ_g, and ϕ_g, as shown in Fig. 2. For the rotation convention used, ψ_g defines rotation about $\hat{\mathbf{z}}$, θ_g defines rotation about $\hat{\mathbf{Y}}_\mathbf{g}$, and ϕ_g defines rotation about $\hat{\mathbf{Z}}_\mathbf{g}$. Now, the coordinate transformation from $\mathbf{X_g}$ to $\mathbf{x}$ can be written as $\mathbf{X_g} = \mathbf{rx}$ where the transformation matrix $\mathbf{r}$ is given by

$$\mathbf{r} = \begin{pmatrix} \cos\psi^g\cos\theta^g\cos\phi^g - \sin\psi^g\sin\phi^g & \sin\psi^g\cos\theta^g\cos\phi^g + \cos\psi^g\sin\phi^g & -\sin\theta^g\cos\phi^g \\ -\cos\psi^g\cos\theta^g\sin\phi^g - \sin\psi^g\cos\phi^g & -\sin\psi^g\cos\theta^g\sin\phi^g + \cos\psi^g\cos\phi^g & \sin\theta^g\sin\phi^g \\ \cos\psi^g\sin\theta^g & \sin\psi^g\sin\theta^g & \cos\theta^g \end{pmatrix}. \tag{18}$$

For the case of rotation about $\hat{\mathbf{z}}$ only, $\boldsymbol{r}$ reduces to

$$\mathbf{r} = \begin{pmatrix} \cos\psi^g & \sin\psi^g & 0 \\ -\sin\psi^g & \cos\psi^g & 0 \\ 0 & 0 & 1 \end{pmatrix}. \tag{19}$$

The vector $\mathbf{q}$ in Eq. (15) can then be modified and written with respect to the coordinate system of the elongated grains, so that $\mathbf{q} = q_{X_g}\hat{\mathbf{X}}_\mathbf{g} + q_{Y_g}\hat{\mathbf{Y}}_\mathbf{g} + q_{Z_g}\hat{\mathbf{Z}}_\mathbf{g}$. Because $\mathbf{X_g} = \mathbf{rx}$ $(X_{g_i} = r_{ij}x_j)$, we have

$$\begin{aligned} q_{X_g} &= \mathbf{q}\cdot\hat{\mathbf{X}}_\mathbf{g} = r_{11}q_x + r_{12}q_y + r_{13}q_z, \\ q_{Y_g} &= \mathbf{q}\cdot\hat{\mathbf{Y}}_\mathbf{g} = r_{21}q_x + r_{22}q_y + r_{23}q_z, \\ q_{Z_g} &= \mathbf{q}\cdot\hat{\mathbf{Z}}_\mathbf{g} = r_{31}q_x + r_{32}q_y + r_{33}q_z, \end{aligned} \tag{20}$$

where the correlation function is now given by

$$\tilde{\eta}(\mathbf{q}) = \frac{a_\mathrm{x}a_\mathrm{y}a_\mathrm{z}}{\pi^2\left(1 + a_\mathrm{x}^2q_{X_g}^2 + a_\mathrm{y}^2q_{Y_g}^2 + a_\mathrm{z}^2q_{Z_g}^2\right)^2}. \tag{21}$$

Finally, for the transducer configuration in Fig. 1 and rotation about only $\hat{\mathbf{z}}$, the correlation function is

$$\tilde{\eta}(\mathbf{q}) = \frac{a_\mathrm{x}a_\mathrm{y}a_\mathrm{z}}{\pi^2\left[1 + k'^2\sin^2\Theta\left(a_\mathrm{x}^2\cos^2\psi_g + a_\mathrm{y}^2\sin^2\psi_g\right) + a_\mathrm{z}^2(k'\cos\Theta + k)^2\right]^2}, \tag{22}$$

which reduces to the expression given by Hu *et al.*[23] for the case of spherical grains ($a_\mathrm{x} = a_\mathrm{y} = a_\mathrm{z} = L$). In Sec. IV, numerical examples are presented for an aluminum sample with arbitrary elongation.

IV. NUMERICAL RESULTS

In order to illustrate the effect of grain elongation, a few numerical examples are presented assuming an aluminum sample with wave speeds $c_L = 6310\,\mathrm{m/s}$ and $c_T = 3070\,\mathrm{m/s}$, density $\rho = 2700\,\mathrm{kg/m^3}$, and single crystal elastic constants $c_{11} = 108\,\mathrm{GPa}$, $c_{12} = 62\,\mathrm{GPa}$, and $c_{44} = 28.3\,\mathrm{GPa}$.[31] These material properties correspond with the sample utilized for the experiments in Sec. V. The transducers are assumed to have matched center frequencies and pulse widths, $\omega_0 = 8\,\mathrm{MHz}$ and $\sigma = 0.17\,\mu\mathrm{s}$, respectively, as well as the same nominal focal lengths and element radii, $F = 50.8\,\mathrm{mm}$ and $a = 4.76\,\mathrm{mm}$. The immersion fluid is selected to be ethylene glycol as in the experiments; for this fluid, the wave speed, density, and attenuation coefficient are $c_f = 1660\,\mathrm{m/s}$, $\rho_f = 1115\,\mathrm{kg/m^3}$ and $\alpha_f = 120\times10^{-3}f^2\,\mathrm{Np/m}$, where f is the frequency in MHz.

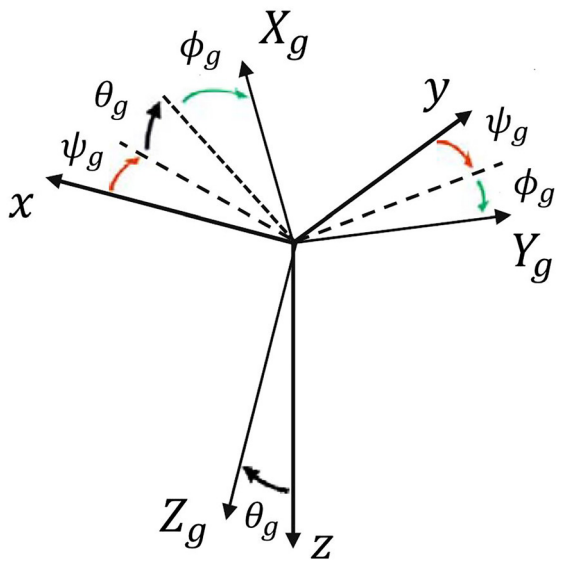

FIG. 2. (Color online) Euler angles used to define the grain coordinate system relative to the fixed reference frame.

For the following two examples, the angle of incidence of the receiving transducer is $\theta_i = 24°$ and the corresponding water paths in order to attain overlapping focal points are $z_{fS} = 20.3$ mm and $z_{fR} = 28.3$ mm for the source and the receiver, respectively. First, we consider the case of grains with elongation in two directions. Constant grain dimensions ($a_x = 15\ \mu$m; $a_y = 60\ \mu$m; $a_z = 30\ \mu$m) are used to evaluate the effect of θ_g on the scattering amplitude. Figure 3 depicts the maximum amplitude of the scattering response $\phi(t)$ as a function of ψ_g. When there is no grain rotation about the Y_g axis ($\theta_g = 0°$), the maximum amplitude occurs at $\psi_g = 0°$ and 180° which corresponds with the oblique transducer (receiver) aligned perpendicular to the direction of elongation (i.e., $\hat{\mathbf{Y}}_\mathbf{g}$ coincides with $\hat{\mathbf{y}}$). The minimum amplitude occurs at $\psi_g = 90°$ when the receiver is aligned with the direction of elongation; this angle represents a point of symmetry in the absence of rotation about $\hat{\mathbf{Y}}_\mathbf{g}$. Rotation by any angle θ_g shifts the minimum amplitude away from $\psi_g = 90°$, disrupting the symmetry; the maximum amplitude then occurs only at $\psi_g = 0°$ (considering rotation $0 < \theta_g < 90°$ due to the symmetry of the grain shape). The largest difference between the amplitudes at $\psi_g = 0$ and $\psi_g = 180°$ corresponds with an angle $\theta_g = 45°$ for which the minimum scattering amplitude occurs at $\psi_g = 101°$. This result illustrates that the direction of grain elongation and presence of grain tilt (relative to the sample surface) can be determined by rotating a sample with respect to a fixed transducer configuration, as the one shown in Fig. 1. The point of maximum scattering amplitude would correspond with the direction perpendicular to elongation and any difference in amplitudes at that point ($\psi_g = 0°$) and $\psi_g = 180°$ would indicate the presence of tilt.

Next the effect of elongation ratio on the mode-converted scattering amplitude is evaluated. Consider grains elongated in the $\hat{\mathbf{Y}}_\mathbf{g}$ direction with circular cross-sections (i.e., $a_x = a_z$). The maximum amplitude of the scattering response as a function of aspect ratio (a_y/a_z) assuming constant grain volume ($V = 4500\pi\ \mu$m^3) is given in Fig. 4 for various values of rotation angle ψ_g between 0° and 90° (the circular cross-section implies symmetry about $\psi_g = 90°$). Increasing the ratio of elongation expectedly increases the maximum ($\psi_g = 0°$) to minimum ($\psi_g = 90°$) amplitude ratio in the response. The scattering amplitude when the receiving transducer is perpendicular to the direction of elongation ($\psi_g = 90°$) rapidly decreases as a function of aspect ratio. In addition, it is observed that the difference in scattering amplitude for $\psi_g = 30°$, 45°, and 90° quickly decreases as function of aspect ratio suggesting greater measurement sensitivity to elongation in smaller ranges of ψ_g for large elongation ratios.

Finally, the effect of the angle of incidence of the receiver is studied. Maintaining a constant grain elongation ratio ($a_x = 15\ \mu$m; $a_y = 75\ \mu$m; $a_z = 15\ \mu$m), the angle of incidence is varied from the first to the second critical angle, $\theta_i = 15.25°$ and 32.73°, respectively. The material path of the source ($z_S = 6.7$ mm) is kept constant and the receiver material path z_R and the distance between the transducers

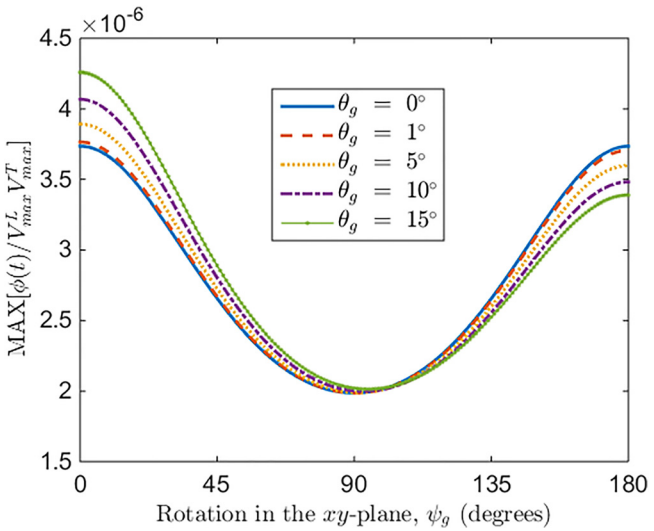

FIG. 3. (Color online) Dependence of the normalized scattering response on tilt angle (θ_g) and rotation angle (ψ_g) of the elongated grains (assuming $a_x = 15\ \mu$m; $a_y = 60\ \mu$m; $a_z = 30\ \mu$m).

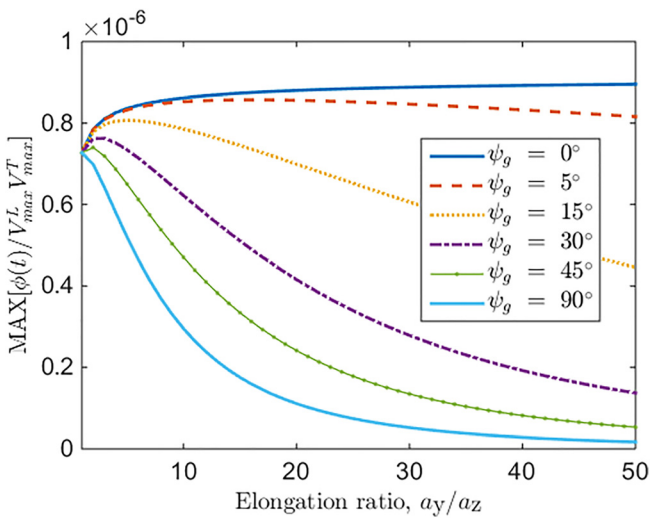

FIG. 4. (Color online) Dependence of the normalized scattering response on aspect ratio of the elongated grains (assuming $a_x = a_z$ and a constant grain volume of $V = 4500\pi\ \mu$m^3.

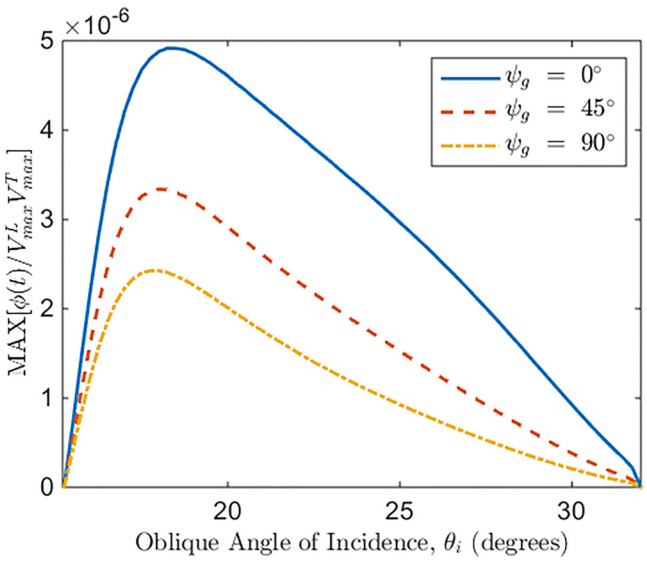

FIG. 5. (Color online) Dependence of the normalized scattering response on the incidence angle of receiver (assuming $a_x = 15\,\mu$m; $a_y = 75\,\mu$m; $a_z = 15\,\mu$m).

($d = z_S \tan\Theta$) are adjusted for each angle of incidence in order to maintain overlapping focal points. Figure 5 shows the change in the maximum amplitude of the scattering response for three rotation angles ψ_g ($\psi_g = 0°$, 90°, and 45°). A sharp increase in the amplitude of the response for all three angles is observed from the first critical angle to a maximum occurring near $\theta_i \approx 18°$, followed by a slower decrease in amplitude to zero at the second critical angle. The ratio of maximum to minimum amplitude ($\psi_g = 0°$ to 90°) increases as the angle of incidence is increased; although the highest amplitude ratio (arguably sensitivity to elongation) is obtained near the second critical angle, the scattering amplitude is low and might fall below the measurement noise. Hence, the optimal experimental setup to maximize sensitivity to elongation is expected to lie between the angle with highest scattering amplitude and the second critical angle. In Sec. V, the procedure and results for ultrasonic experiments conducted on an aluminum 7475 sample are presented along with comparison to the theoretical model in Eq. (11). Grain size estimates are also presented from measurements of electron backscatter diffraction.

V. EXPERIMENTAL RESULTS

Experiments were conducted on a sample of rolled aluminum 7475 with elongated grains to evaluate the validity of the model. The scattered response $\phi(t)$ was measured as the spatial variance of all signals collected within a given region.[22,23] For the experiments, a 100 mm × 100 mm piece of the rolled aluminum was polished to a mirror finish to minimize surface effects. Measurements of wavespeed in all three sample directions were performed using longitudinal and shear contact transducers and the results are shown in Table I. The longitudinal wave speed differs by less than 1% when propagating along the largest grain radius compared with the smallest grain dimension. For shear wave speed, the variation is less than 2.5% which corresponds with wave polarization along a_x and propagation along a_y and a_z. These results confirmed the expected lack of texture within the sample. A pitch-catch configuration was used, as depicted in Fig. 1, with the receiving transducer angle of $\theta_i = 24°$. Ethylene-glycol was used as the coupling fluid to prevent surface deterioration over the course of the experiments. For this couplant, the resulting refraction angle in the solid is approximately $\Theta = 48°$. The material path for the longitudinal transducer, given by $z_S = (F - z_{fS})c_f/c_L$, was chosen to be 6.4 mm with a corresponding receiver material

TABLE I. Experimental results of longitudinal and shear wave speed for rolled aluminum sample along the three principal axes.

Displacement direction ↓	Propagation direction →	a_x	a_y	a_z
= propagation direction	Longitudinal (m/s)	6315.3 ± 6.0	6290.6 ± 0.4	6323.5 ± 7.9
a_x		—	3108.8 ± 0.6	3043.9 ± 0.5
a_y	Shear (m/s)	3094.6 ± 0.3	—	3051.5 ± 10.4
a_z		3046.1 ± 0.3	3079.3 ± 1.6	—

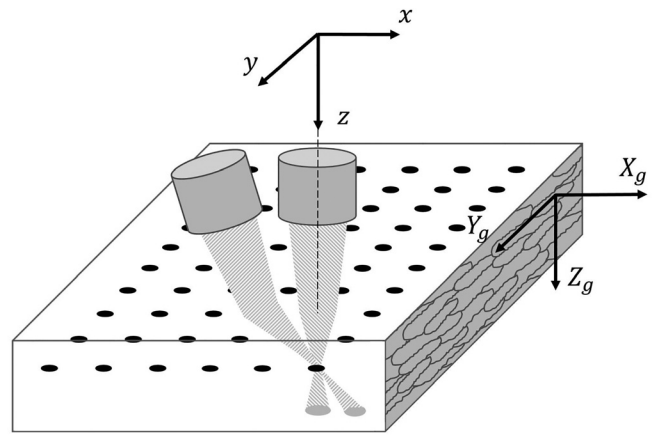

FIG. 6. Schematic of ultrasonic scattering experimental setup for pitch-catch transducer configuration on a sample with elongated grains. The coordinate system **x** coincides with the transducers whereas the coordinate system $\mathbf{X_g}$ corresponds with the grains in the sample.

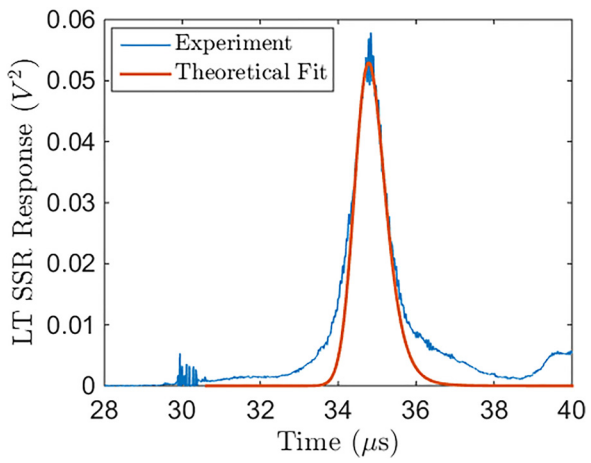

FIG. 7. (Color online) Experimental variance curve for aluminum sample for $\psi_g = 0°$ corresponding to transducers placed perpendicular to the direction of elongation, fitted using SSR model in Eq. (11) with ellipsoidal radii $a_x = 9\,\mu$m; $a_y = 348.9\,\mu$m; $a_z = 1\,\mu$m.

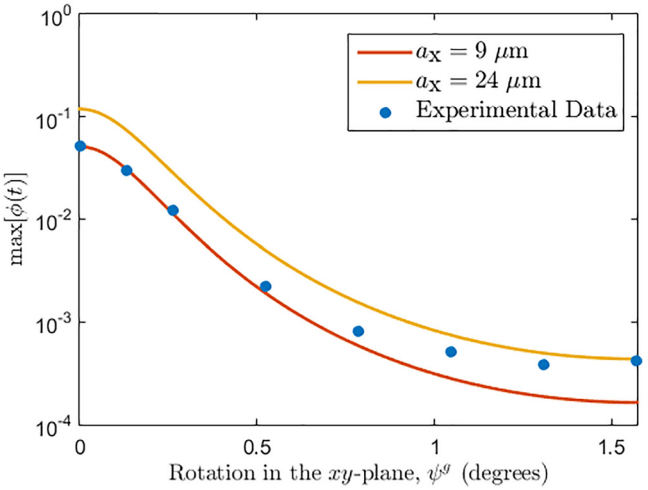

FIG. 8. (Color online) Maximum amplitude of scattered response for experiments conducted at various angles ψ_g and theoretical amplitude obtained using ellipsoidal radii $a_y = 348.9\ \mu m$; $a_z = 1\ \mu m$ with two values of a_x.

path of $z_R = 9.8$ mm resulting in overlapping focal points. Calibration measurements were conducted to obtain V^S_{max} and V^R_{max} on a region of the aluminum sample in accordance with Ghoshal *et al.*[22] Additionally, the transducers (model: Panametrics V327, GE Panametrics, Inc., Waltham, MA; Parameters: 10 MHz, 50.8 mm nominal point target focus, and 9.525 mm element diameter) were calibrated using a steel spherical reflector of 3 mm diameter to determine the pulse widths σ, center frequencies ω_0, and focal lengths F. The pulser/receiver was a DPR300B475-60 (Imaginant and JSR Ultrasonics, Pittsford, NY). The waveforms were collected at a sampling rate of 500 MHz and 50 repetition averages were performed at each spatial position. As depicted in Fig. 6, the pair of transducers was displaced to various positions to collect independent waveforms for the spatial variance. The total area scanned was 60 mm × 60 mm in order to avoid edge effects. The spatial resolution in the y-direction was selected to be 1 mm where as the resolution in the x-direction was selected to be 3 mm to account for the larger spot size in this direction, resulting in a total of 1200 waveforms collected.

An example theoretical fit for the variance of waveforms collected at $\psi_g = 0°$ is shown in Fig. 7, for which grain radii of $a_x = 9\ \mu m$, $a_y = 348.9\ \mu m$, and $a_z = 1\ \mu m$ are used. The sample was then rotated about its $\hat{\mathbf{Z}}_\mathbf{g}$-axis to evaluate the scattering response as a function of ψ_g. Because the amplitudes at $\psi_g = 0°$ and 180° were found to be equal, the data used to extract ellipsoidal grain radii from the model correspond with $0° < \psi_g < 90°$. For this process, the rest of the experimental variance curves were fit using a Gaussian distribution function and the peak amplitudes were then compared to peak amplitudes of the SSR model obtained using different values of a_x, a_y, and a_z. The optimal model radii were extracted by minimizing the least squares error between the model and the experiments. This approach yielded $a_x = 9\ \mu m$; $a_y = 348.9\ \mu m$; $a_z = 1\ \mu m$; the scattering response according to the model as a function of ψ_g as well as the experimental variance peak amplitudes are given in Fig. 8. This figure shows that when using these grain radii the error is small near $\psi^g = 0°$ but increases as ψ^g approached 90°. In order to illustrate the error at the smaller angles when optimizing the fit at $\psi^g = 90°$, the radius a_x was increased to 24 μm. With the new grain radii, the error at the smaller angles increases.

The sample was then characterized using electron backscatter diffraction (EBSD) to obtain representative dimensions

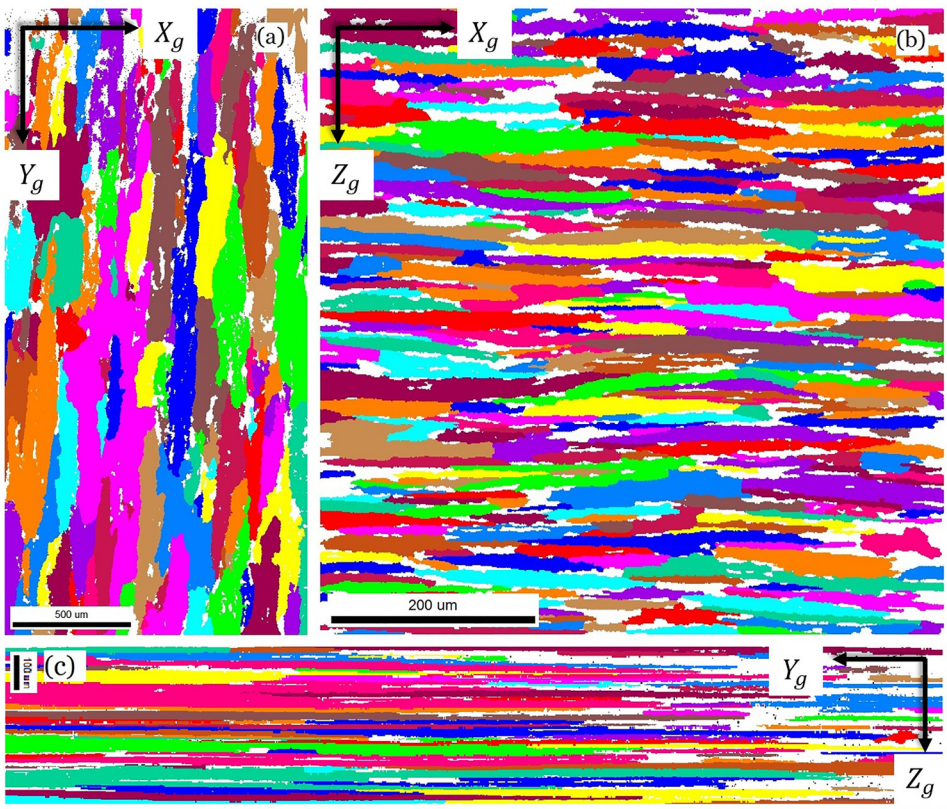

FIG. 9. (Color online) Electron backscatter diffraction (EBSD) unique grain maps for (a) X_gY_g cross section of the sample, (b) X_gZ_g cross section of the sample, and (c) Y_gZ_g cross section of the sample.

of the grains. Small square segments of the three cross-sections of the sample were polished using increasing grit size of silicon carbide paper followed by diamond polishing and 50 nm colloidal silica. The samples were etched using Keller's reagent before imaging. Grain sizing was performed following ISO 13067 using OIM data analysis software. Figure 9 depicts the grain maps used for data analysis; the colors correspond with unique grains defined by crystallographic misorientation greater than 10°. Note that these maps are not representative of texture in the material as the individual colors do not correspond with a particular grain orientation; white spaces in the maps correspond with areas with an insufficient number of points properly indexed (more than 100 indexed points were required for a given area to be considered a grain). Imaging of the Y_gZ_g cross section was challenging given the very large aspect ratio of the grains. Hence, this area was excluded from the analysis. Histograms of grain radii by area fraction were obtained using the software, then the radii with highest percent area were selected yielding $a_x = 49.5\ \mu$m, $a_y = 326.8\ \mu$m, $a_z = 6.1\ \mu$m.

When using the least squares error between the theory and experimental scattering amplitudes, estimates for the grains ellipsoidal radii obtained through the mode-converted SSR model were closest for the largest radius (a_y estimated within 25 μm of EBSD). The largest error was obtained for the in-plane radius; when optimizing the parameters for the higher rotation angles ($\psi^g = 90°$) the estimate of this radius is close ($a_x = 24\ \mu$m for SSR compared with $a_x = 49.5\ \mu$m for EBSD). This result suggests that utilizing separate scattering directions for each grain radius may be a better approach for grain size estimates. Additionally, a combination of different scattering modes (longitudinal-to-longitudinal, shear-to-shear, and mode-converted) could provide more detailed information about all grain radii.

VI. SUMMARY

In this article, a mode-converted scattering model was derived to quantify grain size and elongation in polycrystalline media from experimental measurements made as a function of rotation angle. This work is an extension of the model by Hu *et al.*[23] which describes the portion of the longitudinal wave energy that scatters into transverse energy in polycrystalline media with equiaxed grains. Numerical results for rolled aluminum were presented and the results illustrated possible experimental configurations that could be used to extract grain radii and orientation efficiently. Experimental data collected from a 7475 aluminum sample were fit using the model for several measurement angles. A least squares optimization routine was used to extract the average grain radii. These results were then compared to grain dimensions extracted through electron backscatter diffraction (EBSD) measurements. Using the model to extract ellipsoidal radii from experiments conducted on a single surface of the sample proved highly effective in estimating the largest radius (a_y) and the radius in the direction of wave propagation (a_z). The specific measurement configuration used here resulted in poor estimates of the second in-plane radius (a_x) when compared with the EBSD data. The reasons behind this deficiency are not yet clear. However, the numerical results from the model showed that the experimental configurations can be optimized by considering the frequency, scattering angle, and material path dependence such that all three dimensions may be estimated more reliably. The mode-converted scattering approach has many positive aspects that are expected to provide new opportunities for microstructural characterization of heterogeneous materials.

ACKNOWLEDGMENTS

The support of Luz Sotelo and Mak Koten is gratefully acknowledged for the sample preparation and EBSD measurements.

APPENDIX

The inner product found in Eq. (14) can be written in terms of products of single-crystal elastic constants and the angle formed between the incident and scattering directions. For the transducer configuration given in Fig. 1, the inner product will have the general form

$$\Xi^{\alpha\beta\gamma\delta}_{mnop}\hat{e}_m\hat{k}_n\hat{e}'_o\hat{k}'_p\hat{e}_\alpha\hat{k}_\beta\hat{e}'_\gamma\hat{k}'_\delta = A_0 + A_1\cos 4\Theta, \tag{A1}$$

where Θ is the angle between the incident and scattered waves in the material. For crystallites having triclinic crystallographic symmetry the constants A_0 and A_1 are

$$\begin{aligned}A_0 = \frac{1}{12\,600}\big[&212c_{11}^2 - 64c_{11}c_{12} - 64c_{11}c_{13} - 131c_{11}c_{34} - 34c_{11}c_{35} - 131c_{11}c_{44}\\ &- 228c_{11}c_{46} - 48c_{11}c_{55} - 48c_{11}c_{66} + 167c_{12}^2 - 86c_{12}c_{13} - 64c_{12}c_{34} - 86c_{12}c_{35}\\ &- 34c_{12}c_{44} - 12c_{12}c_{46} - 12c_{12}c_{55} + 348c_{12}c_{66} + 167c_{13}^2 - 34c_{13}c_{34} - 86c_{13}c_{35}\\ &- 64c_{13}c_{44} - 12c_{13}c_{46} + 348c_{13}c_{55} - 12c_{13}c_{66} + 420c_{33}^2 - 60c_{33}c_{36} - 60c_{33}c_{45}\\ &+ 720c_{33}c_{56} + 212c_{34}^2 - 64c_{34}c_{35} - 131c_{34}c_{44} - 48c_{34}c_{46} - 228c_{34}c_{55} - 48c_{34}c_{66}\\ &+ 167c_{35}^2 - 64c_{35}c_{44} + 348c_{35}c_{46} - 12c_{35}c_{55} - 12c_{35}c_{66} + 960c_{36}^2 + 300c_{36}c_{45}\\ &+ 360c_{36}c_{56} + 212c_{44}^2 - 48c_{44}c_{46} - 48c_{44}c_{55} - 228c_{44}c_{66} + 960c_{45}^2 + 360c_{45}c_{56}\\ &+ 588c_{46}^2 - 264c_{46}c_{55} - 264c_{46}c_{66} + 588c_{55}^2 - 264c_{55}c_{66} + 1440c_{56}^2 + 588c_{66}^2\big],\end{aligned}$$

$$A_1 = \frac{1}{12\,600}\big[-12c_{11}^2 + 24c_{11}c_{12} + 24c_{11}c_{13} + 11c_{11}c_{34} - 46c_{11}c_{35} + 11c_{11}c_{44} + 68c_{11}c_{46} - 32c_{11}c_{55} - 32c_{11}c_{66} - 47c_{12}^2 + 46c_{12}c_{13} + 24c_{12}c_{34} + 46c_{12}c_{35} - 46c_{12}c_{44} - 68c_{12}c_{46} - 68c_{12}c_{55} + 132c_{12}c_{66} - 47c_{13}^2 - 46c_{13}c_{34} + 46c_{13}c_{35} + 24c_{13}c_{44} - 68c_{13}c_{46} + 132c_{13}c_{55} - 68c_{13}c_{66} - 140c_{33}^2 + 140c_{33}c_{36} + 140c_{33}c_{45} + 400c_{33}c_{56} - 12c_{34}^2 + 24c_{34}c_{35} + 11c_{34}c_{44} - 32c_{34}c_{46} + 68c_{34}c_{55} - 32c_{34}c_{66} - 47c_{35}^2 + 24c_{35}c_{44} + 132c_{35}c_{46} - 68c_{35}c_{55} - 68c_{35}c_{66} - 40c_{36}^2 - 60c_{36}c_{45} - 200c_{36}c_{56} - 12c_{44}^2 - 32c_{44}c_{46} - 32c_{44}c_{55} + 68c_{44}c_{66} - 40c_{45}^2 - 200c_{45}c_{56} - 108c_{46}^2 + 104c_{46}c_{55} + 104c_{46}c_{66} - 108c_{55}^2 + 104c_{55}c_{66} - 320c_{56}^2 - 108c_{66}^2\big], \tag{A2}$$

where c_{ij} are the single crystal elastic constants. Triclinic symmetry is the most general of the 32 crystallographic point groups. Inner products for other crystallographic symmetries can be reduced from Eq. (A2) by applying the appropriate symmetry conditions.[32] For crystallites with hexagonal crystallographic symmetry, the constants are

$$A_0 = \frac{1}{12\,600}\big[392c_{11}^2 - 200c_{11}c_{12} - 208c_{11}c_{13} - 376c_{11}c_{33} - 816c_{11}c_{44} + 140c_{12}^2 - 160c_{12}c_{13} + 80c_{12}c_{33} + 240c_{12}c_{44} + 248c_{13}^2 - 128c_{13}c_{33} + 672c_{13}c_{44} + 212c_{33}^2 - 96c_{33}c_{44} + 912c_{44}^2\big],$$

$$A_1 = \frac{1}{12\,600}\big[-72c_{11}^2 + 200c_{11}c_{12} - 112c_{11}c_{13} + 56c_{11}c_{33} + 176c_{11}c_{44} - 140c_{12}^2 + 160c_{12}c_{13} - 80c_{12}c_{33} - 240c_{12}c_{44} - 48c_{13}^2 + 48c_{13}c_{33} + 128c_{13}c_{44} - 12c_{33}^2 - 64c_{33}c_{44} - 112c_{44}^2\big]. \tag{A3}$$

[1]D. Beecham, "Ultrasonic scatter in metals: Its properties and its application to grain size determination," Ultrasonics **4**, 67–76 (1966).
[2]F. J. Margetan, T. A. Gray, and R. B. Thompson, "A technique for quantitative measuring microstructurally induced ultrasonic noise," in *Review of Progress in Quantitative NDE*, edited by D. O. Thompson and D. E. Chimenti (Plenum Press, New York, 1991), Vol. 10, pp. 1721–1728.
[3]R. L. Weaver, "Diffuse field decay for materials characterization," in *Solid Mechanics Research for Quantitative Non-Destructive Evaluation*, edited by J. D. Achenbach and Y. Rajapakse (Martinus Nijhoff, Leiden, the Netherlands, 1987), pp. 425–434.
[4]C. B. Guo, P. Holler, and K. Goebbels, "Scattering of ultrasonic waves in anisotropic polycrystalline metals," Acustica **59**, 112–120 (1985).
[5]R. L. Weaver, "Ultrasonic diffuse field measurements of grain size," in *NonDestructive Testing and Evaluation in Manufacturing and Construction*, edited by H. L. M. D. Reis (Hemisphere, New York, 1990), pp. 425–434.
[6]J. H. Rose, "Ultrasonic backscattering from polycrystalline aggregates using time-domain linear response theory," in *Review of Progress in Quantitative NDE*, edited by D. O. Thompson and D. E. Chimenti (Plenum Press, New York, 1991), Vol. 10, pp. 1715–1720.
[7]J. H. Rose, "Ultrasonic backscatter from microstructure," in *Review of Progress in Quantitative NDE*, edited by D. O. Thompson and D. E. Chimenti (Plenum Press, New York, 1992), Vol. 11, pp. 1677–1684.
[8]J. H. Rose, "Theory of ultrasonic backscatter from multiphase polycrystalline solids," in *Review of Progress in Quantitative NDE*, edited by D. O. Thompson and D. E. Chimenti (Plenum Press, New York, 1993), Vol. 12, pp. 1719–1726.
[9]F. J. Margetan, R. B. Thompson, and I. Yalda-Mooshabad, "Backscattered microstructural noise in ultrasonic toneburst inspections," J. Nondestruct. Eval. **13**, 111–136 (1994).
[10]S. Ahmed and R. B. Thompson, "Influence of columnar microstructure on ultrasonic backscattering," in *Review of Progress in Quantitative NDE*, edited by D. O. Thompson and D. E. Chimenti (Plenum Press, New York, 1995), Vol. 14, pp. 1617–1624.
[11]Y. K. Han and R. B. Thompson, "Ultrasonic backscattering in duplex microstructures: Theory and application to titanium alloys," Metallurg. Trans. A. **28**, 91–104 (1997).
[12]Y. Guo, R. B. Thompson, D. K. Rehbein, and F. J. Margetan, "The effects of microstructure on the response of aluminum E-127 calibration standards," in *Review of Progress in Quantitative NDE*, edited by D. O. Thompson and D. E. Chimenti (Plenum Press, New York, 1999), Vol. 18, pp. 2337–2344.
[13]Y. Guo, R. B. Thompson, and F. J. Margetan, "Simultaneous measurement of grain size and shape from ultrasonic backscattering measurements made from a single surface," in *Review of Progress in Quantitative NDE*, edited by D. O. Thompson and D. E. Chimenti (AIP, New York, 2003), Vol. 22, pp. 1347–1354.
[14]O. I. Lobkis and S. I. Rokhlin, "Characterization of polycrystals with elongated duplex microstructure by inversion of ultrasonic backscattering data," Appl. Phys. Lett. **96**, 161905 (2010).
[15]O. I. Lobkis, L. Yang, J. Li, and S. I. Rokhlin, "Ultrasonic backscattering in polycrystals with elongated single phase and duplex microstructures," Ultrasonics. **52**, 694–705 (2012).
[16]L. Yang, J. Li, O. I. Lobkis, and S. I. Rokhlin, "Ultrasonic propagation and scattering in duplex microstructures with application to titanium alloys," J. Nondestruct. Eval. **31**, 270–283 (2012).
[17]L. Yang, O. I. Lobkis, and S. I. Rokhlin, "An integrated model for ultrasonic wave propagation and scattering in a polycrystalline medium with elongated hexagonal grains," Wave Motion **49**, 544–560 (2012).
[18]L. Yang, J. Li, and S. I. Rokhlin, "Ultrasonic scattering in polycrystals with orientation clusters of orthorhombic crystallites," Wave Motion **50**, 1283–1302 (2013).
[19]L. Yang and S. I. Rokhlin, "Ultrasonic backscattering in cubic polycrystals with ellipsoidal grains and texture," J. Nondestruct. Eval. **32**, 142–155 (2013).
[20]J. Li, L. Yang, and S. I. Rokhlin, "Effect of texture and grain shape on ultrasonic backscattering in polycrystals," Ultrasonics **54**, 1789–1803 (2014).
[21]G. Ghoshal, J. A. Turner, and R. L. Weaver, "Wigner distribution function of a transducer beam pattern within a multiple scattering formalism for heterogeneous solids," J. Acoust. Soc. Am. **122**, 2009–2021 (2007).
[22]G. Ghoshal and J. A. Turner, "Diffuse ultrasonic backscatter at normal incidence through a curved interface," J. Acoust. Soc. Am. **128**, 3449–3458 (2010).
[23]P. Hu, C. M. Kube, L. W. Koester, and J. A. Turner, "Mode-converted diffuse ultrasonic backscatter," J. Acoust. Soc. Am. **134**, 982–990 (2013).
[24]R. L. Weaver, "Diffusivity of ultrasound in polycrystals," J. Mech. Phys. Solids. **38**, 55–86 (1990).
[25]L. W. Schmerr and S. J. Song, *Ultrasonic Nondestructive Evaluation System* (Springer, New York, 2007), pp. 507–522.

[26]C. M. Kube and J. A. Turner, "Acoustic attenuation coefficients for polycrystalline materials containing crystallites of any symmetry class," J. Acoust. Soc. Am. **137**(6), EL476–EL482 (2015).
[27]R. B. Thompson and E. F. Lopes, "The effects of focusing and refraction on Gaussian ultrasonic beams," J. Nondestruct. Eval. **4**, 107–123 (1984).
[28]P. H. Rogers and A. L. Van Buren, "An exact expression for the Lommel diffraction correction integral," J. Acoust. Soc. Am. **55**, 724–728 (1974).
[29]J. A. Turner and R. L. Weaver, "Radiative transfer and multiple scattering of diffuse ultrasound in polycrystalline media," J. Acoust. Soc. Am. **96**, 3675–3683 (1994).
[30]F. J. Margetan, L. Yu, and R. B. Thompson, "Computation of grain noise scattering coefficients for ultrasonic pitch/catch inspection of metals," in *Review of Progress in Quantitative NDE*, edited by D. O. Thompson and D. E. Chimenti (Plenum Press, New York, 2005), Vol. 24B, pp. 1300–1307.
[31]A. G. Every and A. K. McCurdy, "Second and higher order elastic constants," Landolt-Bornstein Numerical Data and Functional Relationships in Science and Technology New Series Group III, 29a (Springer-Verlag, Berlin, 1992).
[32]K. Brugger, "Pure modes for elastic waves in crystals," J. Appl. Phys. **36**, 759–768 (1965).